

# Trajectory Planning Under Stochastic and Bounded Sensing Uncertainties Using Reachability Analysis

Akshay Shetty, University of Illinois Urbana-Champaign  
Grace Xingxin Gao, Stanford University

**Akshay Shetty** is a Ph.D. candidate in the Department of Aerospace Engineering at University of Illinois at Urbana-Champaign, and a visiting scholar at Stanford University. He received his M.S. degree in Aerospace Engineering from University of Illinois at Urbana-Champaign in 2017, and his B.Tech. degree in Aerospace Engineering from Indian Institute of Technology, Bombay, India in 2014. His research interests include safety, trajectory planning, and control for autonomous vehicles.

**Grace Xingxin Gao** Grace Xingxin Gao is an assistant professor in the Department of Aeronautics and Astronautics at Stanford University. Before joining Stanford University, she was an assistant professor at University of Illinois at Urbana-Champaign. She obtained her Ph.D. degree at Stanford University. Her research is on robust and secure positioning, navigation and timing with applications to manned and unmanned aerial vehicles, robotics, and power systems.

## Abstract

Trajectory planning under uncertainty is an active research topic. Previous works predict state and state estimation uncertainties along trajectories to check for collision safety. They assume *either* stochastic *or* bounded sensing uncertainties. However, GNSS pseudoranges are typically modeled to contain stochastic uncertainties with additional biases in urban environments. Thus, given bounds for the bias, the planner needs to account for *both* stochastic *and* bounded sensing uncertainties. In our prior work [1] we presented a reachability analysis to predict state and state estimation uncertainties under stochastic and bounded uncertainties. However, we ignored the correlation between these uncertainties, leading to an imperfect approximation of the state uncertainty. In this paper we improve our reachability analysis by predicting state uncertainty as a function of independent quantities. We design a metric for the predicted uncertainty to compare candidate trajectories during planning. Finally, we validate the planner for GNSS-based urban navigation of fixed-wing UAS.

## Keywords

**Trajectory Planning, Reachability Analysis, Probabilistic Zonotope, Global Navigation Satellite System (GNSS), Unmanned Aerial System (UAS)**

## I. INTRODUCTION

Recently there has been growing interest in autonomous applications of robotic systems for various purposes such as delivering goods, surveying areas of interest, and search and rescue [2]–[6]. In general the problem of planning a trajectory for such systems has been extensively explored in literature. Traditional planning approaches proposed rapidly exploring random trees [7] and their variants [8]. However, these works do not account for uncertainty in the system state (position and orientation) that arises due to motion and sensing uncertainties.

Recent works [9]–[12] extended the traditional planners by accounting for motion and sensing uncertainties. These works predict the state uncertainty along candidate trajectories in order to find optimal, collision safe trajectories. In [9] the authors predict the state uncertainty for a system with linear-quadratic-Gaussian (LQG) control, while accounting for sensing uncertainties. The work in [10] predicts a distribution over the system states by considering the state estimation error distribution as well as all possible state estimates that could be realized in the future. In [11] the authors plan trajectories using a velocity obstacle paradigm in combination with a convex approximation of the sensing uncertainties. The work in [12] predicts state uncertainty by using reachability analysis to account for tracking errors of a high-fidelity model in a lower-dimensional planning subspace. However, these works assume *either* a stochastic [9], [10] *or* a bounded [11], [12] sensing uncertainty model, which may not always be valid.

For outdoor navigation, autonomous systems generally use Global Navigation Satellite System (GNSS) measurements for state estimation. GNSS pseudorange measurements are typically modeled to contain stochastic uncertainties along with an additional bias in urban environments due to signal reflections from nearby buildings. These effects are classified either as multipath, where both the direct and reflected signals from the same satellite are received; or as non-line-of-sight (NLOS), where only the reflected satellite signal is received [13]. Generally, NLOS effects result in large biases in pseudorange measurements. Various outlier rejection techniques and three-dimensional (3D) map-based techniques have been proposed to detect and exclude the corresponding measurements [14]–[16]. On the other hand, biases due to multipath effects are relatively lower. Previous works [13], [17] have proposed methods to calculate the bounds for these multipath biases using a 3D map and the GNSS receiver

architecture. Thus, given bounds for the additional bias, the trajectory planner needs to account for the presence of *both* stochastic and bounded sensing uncertainties.

In our prior work [1], we used reachability analysis to predict state uncertainty under motion uncertainty and both stochastic and bounded sensing uncertainties. We recursively predicted the state uncertainty and the state estimation uncertainty, which are functions of the motion and sensing uncertainties along the trajectory. However, we ignored the correlation between the state and the state estimation uncertainties, which led to an imperfect approximation of the state uncertainty. Thus, in this paper we improve our prior reachability analysis and use it within a trajectory planning framework. This paper is based on our work in [18]. The main contributions are listed as follows:

- 1) We discuss the limitations in our prior reachability analysis [1] and present an improved analysis in order to predict state uncertainty as a function of independent (uncorrelated) quantities. We account for the presence of both stochastic and bounded sensing uncertainties in our analysis.
- 2) Next, we combine our method to predict state uncertainty with an available trajectory planning framework [19]. In order to compare candidate trajectories within the planning framework, we design a metric for the size of the predicted state uncertainty.
- 3) Finally, via simulations, we demonstrate the applicability of the trajectory planner for GNSS-based navigation of fixed-wing unmanned aerial systems (UAS) in an urban environment. Planning results are presented for two scenarios: a single UAS in a static environment, and multiple UAS in a shared airspace. We statistically validate the collision safety of the UAS by simulating multiple trajectories along the planned trajectories.

The rest of the paper is organized as follows: we begin by formulating the problem in Section II; in Section III, we present the set representations and operations used in the paper; in Section IV, we mention the limitations of our prior work [1] and discuss our improved reachability analysis used to predict state uncertainty; Section V provides an overview of the trajectory planning framework [19] along with our metric for the size of the predicted state uncertainty; and in Section VI, we demonstrate the planning results for urban GNSS-based navigation of a fixed-wing UAS.

## II. PROBLEM FORMULATION

We consider a non-linear discrete-time system with the following motion model:

$$x_k = f(x_{k-1}, u_{k-1}) + w_k, \quad (1)$$

where  $x_k$  is the state vector,  $u_k$  is the input vector,  $f$  is a non-linear function representing the kinematics,  $w_k$  is the motion model error vector modeled as a zero-mean Gaussian distribution  $\mathcal{N}(0, Q)$ , and  $k$  represents the time instant. For measurements, the following non-linear sensing model is considered:

$$z_k = h(x_k) + \nu_k, \quad (2)$$

where  $z_k$  is the measurement vector,  $h$  is a non-linear function representing the measurements, and  $\nu_k$  is the sensing model error vector modeled as a Gaussian distribution with an uncertain mean, i.e.,  $\mathcal{N}(b_k, R_k)$ . Here the mean  $b_k$  can take any value in a bounded set  $\mathcal{B}_k$ . Thus,  $\nu_k$  captures the presence of both stochastic and bounded sensing uncertainties.

Similar to prior trajectory planning work [10], we assume there exists a low-level CONNECT function that connects a trajectory between two states. Thus, given states  $x^i$  and  $x^j$ , the CONNECT function provides us the following:

$$(\tilde{X}^{i,j}, \tilde{U}^{i,j}, \tilde{K}^{i,j}) = \text{CONNECT}(x^i, x^j), \quad (3)$$

where  $\tilde{X}^{i,j}$  is the set of nominal states  $(\tilde{x}_{\tau_i}, \tilde{x}_{\tau_i+1}, \dots, \tilde{x}_{\tau_j-1})$  and  $\tilde{U}^{i,j}$  is the set of nominal inputs  $(\tilde{u}_{\tau_i}, \tilde{u}_{\tau_i+1}, \dots, \tilde{u}_{\tau_j-1})$ . These nominal states and inputs satisfy the nominal motion model from Equation (1):

$$\begin{aligned} \tilde{x}_k &= f(\tilde{x}_{k-1}, \tilde{u}_{k-1}) \quad \forall k \in [\tau_i + 1, \tau_j - 1], \\ x^i &= \tilde{x}_{\tau_i}, \quad x^j = \tilde{x}_{\tau_j-1}, \end{aligned} \quad (4)$$

where  $\tilde{K}^{i,j}$  is the set of stabilizing linear state feedback control gains  $(\tilde{K}_{\tau_i}, \tilde{K}_{\tau_i+1}, \dots, \tilde{K}_{\tau_j-1})$ . Given the feedback control gain and an on-line state estimate  $\hat{x}_k$ , the total control input during execution is of the form:

$$u_k = \tilde{u}_k - \tilde{K}_k(\hat{x}_k - \tilde{x}_k). \quad (5)$$

Let  $\mathcal{X}^{\text{obs}}$  denote the set of states representing obstacles in the environment. Given an initial state  $x^{\text{init}}$  and a goal state  $x^{\text{goal}}$ , the problem for the trajectory planner is defined as:

$$\begin{aligned} &\min_{(\tilde{X}, \tilde{U}, \tilde{K})} \text{cost}(\tilde{X}, \tilde{U}), \\ &\text{subject to: } \Pr(x_k \in \mathcal{X}^{\text{obs}}) < \delta, \end{aligned} \quad (6)$$

where  $\delta$  is a specified threshold for the probability of collision, and  $(\tilde{X}, \tilde{U}, \tilde{K})$  are concatenated sets representing the nominal trajectory from  $x^{\text{init}}$  to  $x^{\text{goal}}$  as follows:

$$(\tilde{X}, \tilde{U}, \tilde{K}) = (\text{CONNECT}(x^{\text{init}}, x^1), \text{CONNECT}(x^1, x^2), \dots, \text{CONNECT}(x^l, x^{\text{goal}})). \quad (7)$$

For our trajectory planning problem, we set the cost function in Equation (6) to be the total length of the concatenated nominal trajectory from  $x^{\text{init}}$  to  $x^{\text{goal}}$ .

### III. SET REPRESENTATIONS AND OPERATIONS

For our reachability analysis we use probabilistic zonotopes as the set representation since they are suitable to represent both stochastic and bounded sensing uncertainties [20]. Probabilistic zonotopes have been shown to be computationally efficient and closed under linear transform and Minkowski sum operations [21]. A zonotope  $\mathcal{P}$  is defined as follows:

$$\mathcal{P} = \left\{ x \in \mathbb{R}^n \mid x = c_{\mathcal{P}} + \sum_{i=1}^r \beta_i \cdot g_{\mathcal{P}}^{\{i\}}, -1 \leq \beta_i \leq 1 \right\}, \quad (8)$$

where  $c_{\mathcal{P}}$  is the center of the zonotope, and  $g_{\mathcal{P}}^{\{i\}}$  are  $n$ -dimensional column vectors referred to as generators. The generators of a zonotope determine its shape relative to its center. The zonotope can be concisely written as  $\mathcal{P} = \mathcal{Z}(c_{\mathcal{P}}, G_{\mathcal{P}})$ , where  $G_{\mathcal{P}} = [g_{\mathcal{P}}^{\{1\}}, \dots, g_{\mathcal{P}}^{\{r\}}]$  is the corresponding  $n \times r$  generator matrix. Fig. 1(a) shows an example 2D zonotope along with its generator matrix. Zonotopes have been commonly used in literature to represent bounded uncertainties. In [20], the authors extended the representation to include stochastic uncertainties by defining a probabilistic zonotope as a Gaussian distribution with an uncertain and bounded mean:

$$\mathcal{P} = \mathcal{L}(c_{\mathcal{P}}, G_{\mathcal{P}}, \Sigma_{\mathcal{P}}), \quad (9)$$

where  $c_{\mathcal{P}}$  and  $G_{\mathcal{P}}$  represent the zonotope for the bounded uncertainty, and  $\Sigma_{\mathcal{P}}$  is the Gaussian covariance representing the stochastic uncertainty. Fig. 1(b) provides an example visualization of a 2D probabilistic zonotope. Note that probabilistic zonotopes do not have a normalized distribution, and in fact can enclose multiple distributions.

The Minkowski sum operation between two probabilistic zonotopes is defined as [20]:

$$\mathcal{P}_1 \oplus \mathcal{P}_2 = \mathcal{L}(c_{\mathcal{P}_1} + c_{\mathcal{P}_2}, [G_{\mathcal{P}_1}, G_{\mathcal{P}_2}], \Sigma_{\mathcal{P}_1} + \Sigma_{\mathcal{P}_2}), \quad (10)$$

whereas, the linear transform operation is defined as [20]:

$$T \cdot \mathcal{P} = \mathcal{L}(Tc_{\mathcal{P}}, TG_{\mathcal{P}}, T\Sigma_{\mathcal{P}}T^{\top}). \quad (11)$$

Note that the Minkowski sum operation in Equation (10) assumes  $\mathcal{P}_1$  and  $\mathcal{P}_2$  to be independent probabilistic zonotopes as it does not consider the correlation between the corresponding Gaussian covariances  $\Sigma_{\mathcal{P}_1}$  and  $\Sigma_{\mathcal{P}_2}$ . This property gives rise to the limitation in our prior work and hence motivates our approach for computing stochastic reachable sets as discussed later in Section IV-C.

### IV. REACHABILITY ANALYSIS

In this section, we present our reachability analysis used to predict the state uncertainty. We first briefly describe the state estimation filter used on-board. Next, we address the limitation in our prior reachability analysis, and derive the equations for

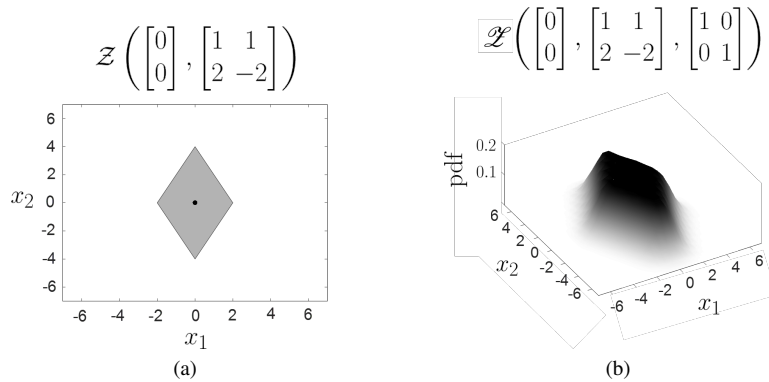


Fig. 1: Example 2D visualizations of (a) a zonotope, and (b) a probabilistic zonotope.

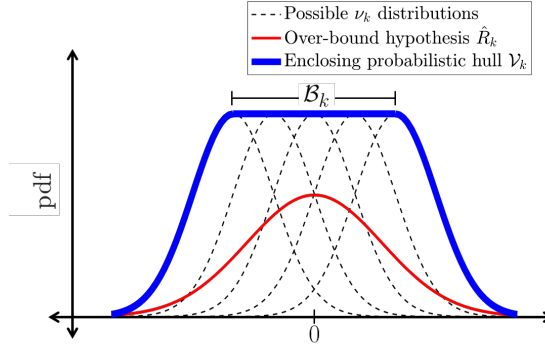


Fig. 2: Visualization of over-bounding hypothesis for the state estimation filter used in the reachability analysis.

computing the stochastic reachable sets as a function of independent quantities. Finally, we discuss the approximations we make to predict the state uncertainty.

#### A. On-board State Estimation

During trajectory execution, the true state  $x_k$  will not be available to compute the control input. Thus, we need to estimate the state  $\hat{x}_k$  in order to compute the total input as shown in Equation (5). Given the non-linear motion and measurement models, we use an EKF as the state estimation filter. The prediction step of the EKF is performed as:

$$\bar{x}_k = f(\hat{x}_{k-1}, u_{k-1}), \quad (12)$$

$$\bar{P}_k = A_k P_{k-1} A_k^\top + Q, \quad (13)$$

where  $A_k = \frac{\partial f}{\partial x} \Big|_{x=\bar{x}_k}$  and  $Q$  is the covariance of the motion model uncertainty defined in Equation (1). For the EKF correction step, similar to our prior work, we choose an over-bounding hypothesis  $\hat{R}_k$  as the measurement covariance matrix. The over-bounding is performed such that  $\hat{R}_k$  matches the tail of the distribution at a desired confidence level. Fig. 2 illustrates the hypothesis for a simple one-dimensional case. Here, without loss of generality, we assume the sensing model error vector  $\nu_k$  to be centered at origin. Note that our reachability analysis does not necessarily require choosing an over-bounding hypothesis for the EKF measurement covariance matrix. If desired, a different hypothesis can be chosen and used with the rest of the analysis. We choose the over-bounding hypothesis since it is equivalent to scaling or inflating the covariance matrix, which is a common approach for practical implementation of KF and its variants [22]–[24].

Once  $\hat{R}_k$  has been computed, the EKF correction step is performed as:

$$L_k = \bar{P}_k C_k^\top (C_k \bar{P}_k C_k^\top + \hat{R}_k)^{-1}, \quad (14)$$

$$\hat{x}_k = \bar{x}_k + L_k (z_k - h(\bar{x}_k)), \quad (15)$$

$$P_k = \bar{P}_k - L_k C_k \bar{P}_k, \quad (16)$$

where  $L$  is the Kalman gain and  $C_k = \frac{\partial h}{\partial x} \Big|_{x=\hat{x}_k}$ .

#### B. Limitations in Our Prior Work

In our prior work we used the system equations (1)–(5) and state estimation equations (12)–(16) to derive the following recursive equations for the state  $x_k$  and state estimation error  $\tilde{x}_k (= \hat{x}_k - x_k)$ :

$$x_k = (A_{k-1} - B_{k-1} \tilde{K}_{k-1})(x_{k-1} - \tilde{x}_{k-1}) - B_{k-1} \tilde{K}_{k-1} \tilde{x}_{k-1} + \tilde{x}_k + \mathcal{L}_{[s, \tilde{s}]_{k-1}}^f + w_k, \quad (17)$$

$$\tilde{x}_k = (I - L_k C_k) A_{k-1} \tilde{x}_{k-1} + (I - L_k C_k) (\mathcal{L}_{[\tilde{s}, \tilde{s}]_{k-1}}^f - \mathcal{L}_{[s, \tilde{s}]_{k-1}}^f) + L_k (\mathcal{L}_{[x, \tilde{x}]_k}^h - \mathcal{L}_{[\bar{x}, \tilde{x}]_k}^h) - (I - L_k C_k) w_k + L_k \nu_k, \quad (18)$$

where  $s^\top = [x^\top, u^\top]$  and  $\mathcal{L}$  are Lagrange remainders resulting from the linearization of the non-linear models. For instance the remainder  $\mathcal{L}_{[s, \tilde{s}]_{k-1}}^f$  is expressed as:

$$\begin{aligned} \mathcal{L}_{[s, \tilde{s}]_{k-1}}^{f(i)} &= \frac{1}{2} (s_{k-1} - \tilde{s}_{k-1})^\top J_s^{f(i)}(\xi) (s_{k-1} - \tilde{s}_{k-1}), \\ \xi &\in \{\tilde{s}_{k-1} + \eta(s_{k-1} - \tilde{s})_{k-1} \mid \eta \in [0, 1]\}, \end{aligned} \quad (19)$$

where subscript  $(i)$  represents the  $i^{th}$  element of the remainder vector and  $J_s^{f(i)}(\xi) = \frac{\partial^2 f(i)(\xi)}{\partial s^2}$ .

We then extended Equations (17) and (18) to set notations in order to recursively compute the stochastic reachable set  $\mathcal{X}_k$  and the state estimation error set  $\tilde{\mathcal{X}}_k$ :

$$\mathcal{X}_k = (A_{k-1} - B_{k-1}\tilde{K}_{k-1})(\mathcal{X}_{k-1} - \tilde{x}_{k-1}) \oplus B_{k-1}\tilde{K}_{k-1}\tilde{\mathcal{X}}_{k-1} + \tilde{x}_k \oplus \mathcal{L}_{[s,\tilde{s}]_{k-1}}^f \oplus \mathcal{W}_k, \quad (20)$$

$$\tilde{\mathcal{X}}_k = (I - L_k C_k)A_{k-1}\tilde{\mathcal{X}}_{k-1} \oplus (I - L_k C_k)(\mathcal{L}_{[\hat{s},\tilde{s}]_{k-1}}^f \oplus \mathcal{L}_{[s,\tilde{s}]_{k-1}}^f) \oplus L_k(\mathcal{L}_{[x,\tilde{x}]_k}^h \oplus \mathcal{L}_{[\bar{x},\tilde{x}]_k}^h) \oplus (I - L_k C_k)\mathcal{W}_k \oplus L_k \mathcal{V}_k, \quad (21)$$

where  $\mathcal{W}_k$  and  $\mathcal{V}_k$  are the set representations for uncertainties in the motion and sensing models, respectively. However, for the first Minkowski sum operation in Equation (20) the sets  $\mathcal{X}_{k-1}$  and  $\tilde{\mathcal{X}}_{k-1}$  are not independent. By rewriting Equations (20) and (21) for the previous time instant, we observe that both  $\mathcal{X}_{k-1}$  and  $\tilde{\mathcal{X}}_{k-1}$  depend on  $\mathcal{W}_{k-1}$ . Thus, ignoring the correlation between  $\mathcal{X}_{k-1}$  and  $\tilde{\mathcal{X}}_{k-1}$  results in an imperfect approximation of the stochastic reachable set  $\mathcal{X}_k$ .

### C. Improved Computation of Stochastic Reachable Sets

In order to avoid the imperfect approximation in our prior work, we first derive equations for the state and the state estimation error as a function of independent (and hence uncorrelated) quantities. This is in contrast to Equation (17) where  $x_{k-1}$  and  $\tilde{x}_{k-1}$  are correlated. We then extend the equations to set notations in order to compute the stochastic reachable set and the state estimation error set. Since the corresponding sets represent independent quantities, the Minkowski sum operations do not result in an imperfect approximation, in contrast to Equation (20).

We prove using mathematical induction that the state  $x_k$  and the state estimation error  $\tilde{x}_k$  can be obtained as a function of independent quantities as follows:

$$x_k = \tilde{x}_k + {}^1\phi_k(x_0 - \tilde{x}_0) + {}^2\phi_k\tilde{x}_0 + \sum_{n=1}^k {}^3\phi_k^n w_n + \sum_{n=1}^k {}^4\phi_k^n \nu_n + \sum_{n=0}^{k-1} {}^5\phi_k^n \mathcal{L}_{[s,\tilde{s}]_n}^f + \sum_{n=0}^{k-1} {}^6\phi_k^n \mathcal{L}_{[\hat{s},\tilde{s}]_n}^f + \sum_{n=0}^{k-1} {}^7\phi_k^n \mathcal{L}_{[x,\tilde{x}]_n}^h + \sum_{n=0}^{k-1} {}^8\phi_k^n \mathcal{L}_{[\bar{x},\tilde{x}]_n}^h, \quad (22)$$

$$\tilde{x}_k = {}^2\tilde{\phi}_k\tilde{x}_0 + \sum_{n=1}^k {}^3\tilde{\phi}_k^n w_n + \sum_{n=1}^k {}^4\tilde{\phi}_k^n \nu_n + \sum_{n=0}^{k-1} {}^5\tilde{\phi}_k^n \mathcal{L}_{[s,\tilde{s}]_n}^f + \sum_{n=0}^{k-1} {}^6\tilde{\phi}_k^n \mathcal{L}_{[\hat{s},\tilde{s}]_n}^f + \sum_{n=0}^{k-1} {}^7\tilde{\phi}_k^n \mathcal{L}_{[x,\tilde{x}]_n}^h + \sum_{n=0}^{k-1} {}^8\tilde{\phi}_k^n \mathcal{L}_{[\bar{x},\tilde{x}]_n}^h, \quad (23)$$

where all  $\phi_k$  and  $\tilde{\phi}_k$  are matrix coefficients derived from system and state estimation matrices. Here  $x_0$  is the initial state of the system,  $\tilde{x}_0$  is the initial state estimation error,  $w_n$  and  $\nu_n$  are motion and sensing model errors independently sampled along the trajectory, and  $\mathcal{L}$  are the Lagrange remainders.

*Proof:* For the induction base case, the initial state and state estimation error can be written in the above form as:

$$\begin{aligned} x_0 &= \tilde{x}_0 + (x_0 - \tilde{x}_0), \\ \tilde{x}_0 &= \tilde{x}_0, \end{aligned} \quad (24)$$

which can be obtained by setting  ${}^1\phi_0 = I$ ,  ${}^i\phi_0 = O \forall i = \{2, \dots, 8\}$ ,  ${}^2\tilde{\phi}_0 = I$  in Equation (22), and  ${}^i\tilde{\phi}_0 = O \forall i = \{3, \dots, 8\}$  in Equation (23).

For the induction step, we first assume that Equations (22) and (23) hold true for time instant  $k-1$ , i.e.:

$$\begin{aligned} x_{k-1} &= \tilde{x}_{k-1} + {}^1\phi_{k-1}(x_0 - \tilde{x}_0) + {}^2\phi_{k-1}\tilde{x}_0 + \sum_{n=1}^{k-1} {}^3\phi_{k-1}^n w_n + \sum_{n=1}^{k-1} {}^4\phi_{k-1}^n \nu_n + \sum_{n=0}^{k-2} {}^5\phi_{k-1}^n \mathcal{L}_{[s,\tilde{s}]_n}^f \\ &\quad + \sum_{n=0}^{k-2} {}^6\phi_{k-1}^n \mathcal{L}_{[\hat{s},\tilde{s}]_n}^f + \sum_{n=0}^{k-2} {}^7\phi_{k-1}^n \mathcal{L}_{[x,\tilde{x}]_n}^h + \sum_{n=0}^{k-2} {}^8\phi_{k-1}^n \mathcal{L}_{[\bar{x},\tilde{x}]_n}^h, \end{aligned} \quad (25)$$

$$\tilde{x}_{k-1} = {}^2\tilde{\phi}_{k-1}\tilde{x}_0 + \sum_{n=1}^{k-1} {}^3\tilde{\phi}_{k-1}^n w_n + \sum_{n=1}^{k-1} {}^4\tilde{\phi}_{k-1}^n \nu_n + \sum_{n=0}^{k-2} {}^5\tilde{\phi}_{k-1}^n \mathcal{L}_{[s,\tilde{s}]_n}^f + \sum_{n=0}^{k-2} {}^6\tilde{\phi}_{k-1}^n \mathcal{L}_{[\hat{s},\tilde{s}]_n}^f + \sum_{n=0}^{k-2} {}^7\tilde{\phi}_{k-1}^n \mathcal{L}_{[x,\tilde{x}]_n}^h + \sum_{n=0}^{k-2} {}^8\tilde{\phi}_{k-1}^n \mathcal{L}_{[\bar{x},\tilde{x}]_n}^h. \quad (26)$$

Next, in order to show that Equations (22) and (23) hold true for time instant  $k$  we begin by replacing Equation (26) in Equation

(18). This gives us the following expression for the state estimation error  $\tilde{x}_k$ :

$$\begin{aligned}\tilde{x}_k &= (I - L_k C_k) A_{k-1} \tilde{\phi}_{k-1}^2 \tilde{x}_0 + (I - L_k C_k) A_{k-1} \sum_{n=1}^{k-1} \tilde{\phi}_{k-1}^3 w_n - (I - L_k C_k) w_k + (I - L_k C_k) A_{k-1} \sum_{n=1}^{k-1} \tilde{\phi}_{k-1}^4 \nu_n + L_k \nu_k \\ &+ (I - L_k C_k) A_{k-1} \sum_{n=0}^{k-2} \tilde{\phi}_{k-1}^5 \mathcal{L}_{[s, \tilde{s}]_n}^f - (I - L_k C_k) \mathcal{L}_{[s, \tilde{s}]_{k-1}}^f + (I - L_k C_k) A_{k-1} \sum_{n=0}^{k-2} \tilde{\phi}_{k-1}^6 \mathcal{L}_{[\tilde{s}, \tilde{s}]_n}^f + (I - L_k C_k) \mathcal{L}_{[\tilde{s}, \tilde{s}]_{k-1}}^f \\ &+ (I - L_k C_k) A_{k-1} \sum_{n=0}^{k-2} \tilde{\phi}_{k-1}^7 \mathcal{L}_{[x, \tilde{x}]_n}^h + L_k \mathcal{L}_{[x, \tilde{x}]_k}^h + (I - L_k C_k) A_{k-1} \sum_{n=0}^{k-2} \tilde{\phi}_{k-1}^8 \mathcal{L}_{[\tilde{x}, \tilde{x}]_n}^h - L_k \mathcal{L}_{[\tilde{x}, \tilde{x}]_k}^h.\end{aligned}\quad (27)$$

The above equation can then be written in the form of Equation (23) where the  $\tilde{\phi}_k$  matrix coefficients can be obtained as:

$$\begin{aligned}\tilde{\phi}_k^2 &= (I - L_k C_k) A_{k-1} \tilde{\phi}_{k-1}^2, \\ \tilde{\phi}_k^{3n} &= (I - L_k C_k) A_{k-1} \tilde{\phi}_{k-1}^{3n} \quad \forall n \in \{1, \dots, k-1\}, \quad \tilde{\phi}_k^{3k} = -(I - L_k C_k), \\ \tilde{\phi}_k^{4n} &= (I - L_k C_k) A_{k-1} \tilde{\phi}_{k-1}^{4n} \quad \forall n \in \{1, \dots, k-1\}, \quad \tilde{\phi}_k^{4k} = L_k, \\ \tilde{\phi}_k^{5n} &= (I - L_k C_k) A_{k-1} \tilde{\phi}_{k-1}^{5n} \quad \forall n \in \{0, \dots, k-2\}, \quad \tilde{\phi}_k^{5k-1} = -(I - L_k C_k), \\ \tilde{\phi}_k^{6n} &= (I - L_k C_k) A_{k-1} \tilde{\phi}_{k-1}^{6n} \quad \forall n \in \{0, \dots, k-2\}, \quad \tilde{\phi}_k^{6k-1} = (I - L_k C_k), \\ \tilde{\phi}_k^{7n} &= (I - L_k C_k) A_{k-1} \tilde{\phi}_{k-1}^{7n} \quad \forall n \in \{0, \dots, k-2\}, \quad \tilde{\phi}_k^{7k-1} = L_k, \\ \tilde{\phi}_k^{8n} &= (I - L_k C_k) A_{k-1} \tilde{\phi}_{k-1}^{8n} \quad \forall n \in \{0, \dots, k-2\}, \quad \tilde{\phi}_k^{8k-1} = -L_k.\end{aligned}\quad (28)$$

Similarly for state  $x_k$ , replacing Equations (25) and (26) in Equation (17), we get the following expression:

$$\begin{aligned}x_k &= \tilde{x}_k + (A_{k-1} - B_{k-1} \tilde{K}_{k-1})^1 \phi_{k-1} (x_0 - \tilde{x}_0) + \left( (A_{k-1} - B_{k-1} \tilde{K}_{k-1})^2 \phi_{k-1} - B_{k-1} \tilde{K}_{k-1} \tilde{\phi}_{k-1}^2 \right) \tilde{x}_0 + \\ &\sum_{n=1}^{k-1} \left( (A_{k-1} - B_{k-1} \tilde{K}_{k-1})^3 \phi_{k-1}^n - B_{k-1} \tilde{K}_{k-1} \tilde{\phi}_{k-1}^{3n} \right) w_n + w_k + \sum_{n=1}^{k-1} \left( (A_{k-1} - B_{k-1} \tilde{K}_{k-1})^4 \phi_{k-1}^n - B_{k-1} \tilde{K}_{k-1} \tilde{\phi}_{k-1}^{4n} \right) \nu_n + \\ &\sum_{n=0}^{k-2} \left( (A_{k-1} - B_{k-1} \tilde{K}_{k-1})^5 \phi_{k-1}^n - B_{k-1} \tilde{K}_{k-1} \tilde{\phi}_{k-1}^{5n} \right) \mathcal{L}_{[s, \tilde{s}]_n}^f + \mathcal{L}_{[s, \tilde{s}]_{k-1}}^f + \sum_{n=0}^{k-2} \left( (A_{k-1} - B_{k-1} \tilde{K}_{k-1})^6 \phi_{k-1}^n - B_{k-1} \tilde{K}_{k-1} \tilde{\phi}_{k-1}^{6n} \right) \mathcal{L}_{[\tilde{s}, \tilde{s}]_n}^f \\ &+ \sum_{n=0}^{k-2} \left( (A_{k-1} - B_{k-1} \tilde{K}_{k-1})^6 \phi_{k-1}^n - B_{k-1} \tilde{K}_{k-1} \tilde{\phi}_{k-1}^{6n} \right) \mathcal{L}_{[x, \tilde{x}]_n}^h + \sum_{n=0}^{k-2} \left( (A_{k-1} - B_{k-1} \tilde{K}_{k-1})^7 \phi_{k-1}^n - B_{k-1} \tilde{K}_{k-1} \tilde{\phi}_{k-1}^{7n} \right) \mathcal{L}_{[\tilde{x}, \tilde{x}]_n}^h.\end{aligned}\quad (29)$$

The above equation can then be written in the form of Equation (22) where the  $\phi_k$  matrix coefficients can be obtained as:

$$\begin{aligned}\phi_k^1 &= (A_{k-1} - B_{k-1} \tilde{K}_{k-1})^1 \phi_{k-1}, \\ \phi_k^2 &= (A_{k-1} - B_{k-1} \tilde{K}_{k-1})^2 \phi_{k-1} - B_{k-1} \tilde{K}_{k-1} \tilde{\phi}_{k-1}^2, \\ \phi_k^{3n} &= (A_{k-1} - B_{k-1} \tilde{K}_{k-1})^3 \phi_{k-1}^n - B_{k-1} \tilde{K}_{k-1} \tilde{\phi}_{k-1}^{3n} \quad \forall n \in \{1, \dots, k-1\}, \quad \phi_k^{3k} = I, \\ \phi_k^{4n} &= (A_{k-1} - B_{k-1} \tilde{K}_{k-1})^4 \phi_{k-1}^n - B_{k-1} \tilde{K}_{k-1} \tilde{\phi}_{k-1}^{4n} \quad \forall n \in \{1, \dots, k-1\}, \quad \phi_k^{4k} = O, \\ \phi_k^{5n} &= (A_{k-1} - B_{k-1} \tilde{K}_{k-1})^5 \phi_{k-1}^n - B_{k-1} \tilde{K}_{k-1} \tilde{\phi}_{k-1}^{5n} \quad \forall n \in \{0, \dots, k-2\}, \quad \phi_k^{5k-1} = I, \\ \phi_k^{6n} &= (A_{k-1} - B_{k-1} \tilde{K}_{k-1})^6 \phi_{k-1}^n - B_{k-1} \tilde{K}_{k-1} \tilde{\phi}_{k-1}^{6n} \quad \forall n \in \{0, \dots, k-2\}, \quad \phi_k^{6k-1} = O, \\ \phi_k^{7n} &= (A_{k-1} - B_{k-1} \tilde{K}_{k-1})^7 \phi_{k-1}^n - B_{k-1} \tilde{K}_{k-1} \tilde{\phi}_{k-1}^{7n} \quad \forall n \in \{0, \dots, k-2\}, \quad \phi_k^{7k-1} = O, \\ \phi_k^{8n} &= (A_{k-1} - B_{k-1} \tilde{K}_{k-1})^8 \phi_{k-1}^n - B_{k-1} \tilde{K}_{k-1} \tilde{\phi}_{k-1}^{8n} \quad \forall n \in \{0, \dots, k-2\}, \quad \phi_k^{8k-1} = O.\end{aligned}\quad (30)$$

Thus, by the principle of induction, we show that Equations (22) and (23) hold true for all  $k \in \{0, 1, \dots\}$ . The matrix coefficients  $\phi_k$  and  $\tilde{\phi}_k$  are obtained recursively using Equations (28) and (30).  $\blacksquare$

Once the above equations for the state and state estimation errors have been derived, we extend them to set notations in order

to compute the stochastic reachable set  $\mathcal{X}_k$  and the state estimation error set  $\tilde{\mathcal{X}}_k$  as follows:

$$\mathcal{X}_k = \tilde{x}_k \oplus {}^1\phi_k(\mathcal{X}_0 - \tilde{x}_0) \oplus {}^2\phi_k\tilde{\mathcal{X}}_0 \oplus \sum_{n=1}^k {}^3\phi_k^n \mathcal{W}_n \oplus \sum_{n=1}^k {}^4\phi_k^n \mathcal{V}_n \oplus \sum_{n=0}^{k-1} {}^5\phi_k^n \mathcal{L}_{[s,\tilde{s}]_n}^f \oplus \sum_{n=0}^{k-1} {}^6\phi_k^n \mathcal{L}_{[\hat{s},\tilde{s}]_n}^f \oplus \sum_{n=0}^{k-1} {}^7\phi_k^n \mathcal{L}_{[x,\tilde{x}]_n}^h \oplus \sum_{n=0}^{k-1} {}^8\phi_k^n \mathcal{L}_{[\bar{x},\tilde{x}]_n}^h, \quad (31)$$

$$\tilde{\mathcal{X}}_k = {}^2\tilde{\phi}_k\tilde{\mathcal{X}}_0 + \sum_{n=1}^k {}^3\tilde{\phi}_k^n \mathcal{W}_n + \sum_{n=1}^k {}^4\tilde{\phi}_k^n \mathcal{V}_n + \sum_{n=0}^{k-1} {}^5\tilde{\phi}_k^n \mathcal{L}_{[s,\tilde{s}]_n}^f + \sum_{n=0}^{k-1} {}^6\tilde{\phi}_k^n \mathcal{L}_{[\hat{s},\tilde{s}]_n}^f + \sum_{n=0}^{k-1} {}^7\tilde{\phi}_k^n \mathcal{L}_{[x,\tilde{x}]_n}^h + \sum_{n=0}^{k-1} {}^8\tilde{\phi}_k^n \mathcal{L}_{[\bar{x},\tilde{x}]_n}^h. \quad (32)$$

Here the sets  $\mathcal{X}_0$ ,  $\tilde{\mathcal{X}}_0$ ,  $\mathcal{W}_n$ , and  $\mathcal{V}_n$  represent independent quantities and hence the Minkowski sum operations do not result in an imperfect approximation of the stochastic reachable sets.

#### D. Predicting State Uncertainty

Once we have an expression to compute the stochastic reachable sets, we perform the following two approximations in order to predict the state uncertainty:

- 1) We heuristically bound the number of Minkowski sum operations in Equation (31). From Equations (28) and (30) we observe that the matrix coefficients contain contractive terms, which consequently results in some quantities having a negligible contribution in the computation of  $\mathcal{X}_k$ . Thus, we only consider quantities whose corresponding matrix coefficients have a Frobenius norm  $\|\phi_k^n\|_F$  higher than a specified threshold  $\zeta$ .
- 2) We approximate the Lagrange remainders  $\mathcal{L}$  with a Gaussian distribution  $\hat{\mathcal{L}}$ , as presented in our prior work [1].

Thus, we obtain the following expression for the predicted state uncertainty  $\underline{\mathcal{X}}_k$ :

$$\underline{\mathcal{X}}_k = \tilde{x}_k \oplus {}^1\phi_k(\mathcal{X}_0 - \tilde{x}_0) \oplus {}^2\phi_k\tilde{\mathcal{X}}_0 \oplus \sum_{n \in {}^3\mathcal{N}_k} {}^3\phi_k^n \mathcal{W}_n \oplus \sum_{n \in {}^4\mathcal{N}_k} {}^4\phi_k^n \mathcal{V}_n \oplus \sum_{n \in {}^5\mathcal{N}_k} {}^5\phi_k^n \hat{\mathcal{L}}_{1,n}^f \oplus \sum_{n \in {}^6\mathcal{N}_k} {}^6\phi_k^n \hat{\mathcal{L}}_{2,n}^f \oplus \sum_{n \in {}^7\mathcal{N}_k} {}^7\phi_k^n \hat{\mathcal{L}}_{1,n}^h \oplus \sum_{n \in {}^8\mathcal{N}_k} {}^8\phi_k^n \hat{\mathcal{L}}_{2,n}^h, \quad (33)$$

where  ${}^i\mathcal{N}_k$  contains elements  $\{n\}$  such that  $\|\phi_k^n\|_F \geq \zeta$ .

### V. TRAJECTORY PLANNING

#### A. Trajectory Planning Overview

In Section IV we presented our method to predict state uncertainty along a single nominal trajectory. The objective of the trajectory planner is to use this method to explore the environment and find an optimal trajectory for the problem defined in Equation (6). In this paper we choose the planning framework presented in [19] which is desirable given its highly parallelizable structure. However, note that our method to predict state uncertainty can be used with other planning frameworks that consider uncertainty [10], [25].

For details of the trajectory planning framework, we refer the readers to [19]. Here we illustrate the framework in Fig. 3 and summarize it as follows:

- 1) The planner begins with an offline graph constructing phase. Multiple states are sampled in the environment and a graph of kinematically feasible and collision-free trajectories is constructed.
- 2) Next, the planner explores the graph by predicting state uncertainty along candidate trajectories. Intersection between the predicted state uncertainty and the obstacles is checked in order to maintain the desired level of collision safety as specified in Equation (6).
- 3) For computational tractability, the planner removes undesirable trajectories by comparing candidate trajectories that arrive at the same state. Here the comparison is done in terms of the trajectory lengths and the sizes of the predicted state uncertainties.
- 4) Once a collision-safe trajectory to the goal state is found, the planner stops the exploration phase.

Thus, in order to use our method of predicting state uncertainty along with the above planning framework, we need to design a metric to represent the size of the predicted state uncertainty.

#### B. Metric for Predicted State Uncertainty

The state uncertainty along a candidate trajectory is predicted using Equation (33). Given that we use probabilistic zonotopes as our set representation, the state uncertainty can be expressed in the form of Equation (9) as:

$$\underline{\mathcal{X}}_k = \mathcal{Z}(c_{\underline{\mathcal{X}}_k}, G_{\underline{\mathcal{X}}_k}, \Sigma_{\underline{\mathcal{X}}_k}), \quad (34)$$

where  $c_{\underline{\mathcal{X}}_k}$  is the center of the probabilistic zonotope,  $G_{\underline{\mathcal{X}}_k}$  is the generator matrix for the bounded uncertainty, and  $\Sigma_{\underline{\mathcal{X}}_k}$  is the covariance for the stochastic uncertainty.

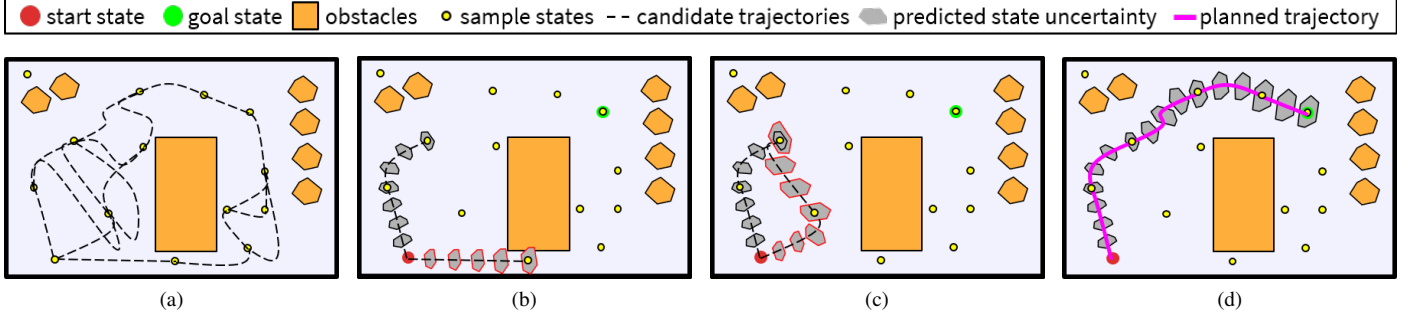


Fig. 3: Overview of trajectory planning framework [19]. (a) The planner first builds a graph of feasible trajectories. Then it explores the graph rejecting (b) collision unsafe and (c) undesirable trajectories. (d) The planner stops exploring once it finds a trajectory to the goal state.

In order to obtain a metric for the size of a probabilistic zonotope, we perform the following steps:

- 1) Generate a confidence zonotope for the state uncertainty as shown in Fig. 4. We represent the confidence zonotope as  $\mathcal{Z}(c_{\text{conf}}, G_{\text{conf}})$ , with center  $c_{\text{conf}} = c_{\mathcal{X}_k}$  and generator matrix:

$$G_{\text{conf}} = [G_{\mathcal{X}_k}, \alpha\sqrt{\lambda_1}v_1, \dots, \alpha\sqrt{\lambda_n}v_n], \quad (35)$$

where  $\alpha$  is a scalar that follows a chi-square distribution [26], [27] based on the collision probability threshold from Equation (6),  $\lambda$  and  $v$  represent the eigenvalues and eigenvectors of the covariance matrix  $\Sigma_{\mathcal{X}_k}$ , and  $n$  here is the dimension of the system.

- 2) Use the covariation of the confidence zonotope as the metric for the size of  $\mathcal{X}_k$ . The covariation of a zonotope is defined as  $\text{trace}(G_{\text{conf}}^\top G_{\text{conf}})$  [28].

## VI. SIMULATIONS

In this section we demonstrate the applicability of the trajectory planner for GNSS-based navigation of fixed-wing UAS in urban environments. We first describe the motion and sensing models we use for the simulations, and then we discuss trajectory planning results for two scenarios: single UAS in a static environment and multiple UAS in a shared airspace.

### A. Motion and Sensing Models

For simplicity we restrict the fixed-wing UAS motion to a horizontal plane and represent it by a 2D Dubins model as follows:

$$\underbrace{\begin{bmatrix} x_{1k} \\ x_{2k} \\ \theta_k \end{bmatrix}}_{x_k} = \underbrace{\begin{bmatrix} x_{1k-1} \\ x_{2k-1} \\ \theta_{k-1} \end{bmatrix} + \begin{bmatrix} V_{k-1} \cos(\theta_{k-1}) \Delta t \\ V_{k-1} \sin(\theta_{k-1}) \Delta t \\ \omega_{k-1} \Delta t \end{bmatrix}}_{f(x_{k-1}, u_{k-1})} + w_k, \quad (36)$$

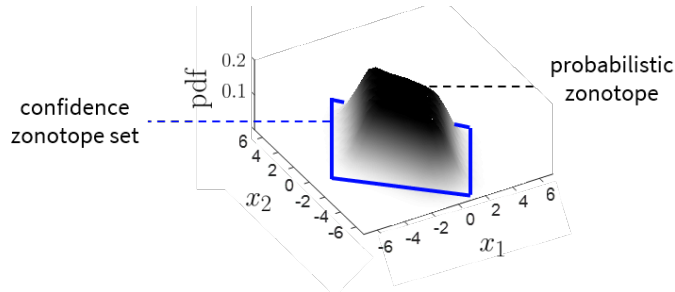


Fig. 4: Confidence zonotope of a probabilistic zonotope.



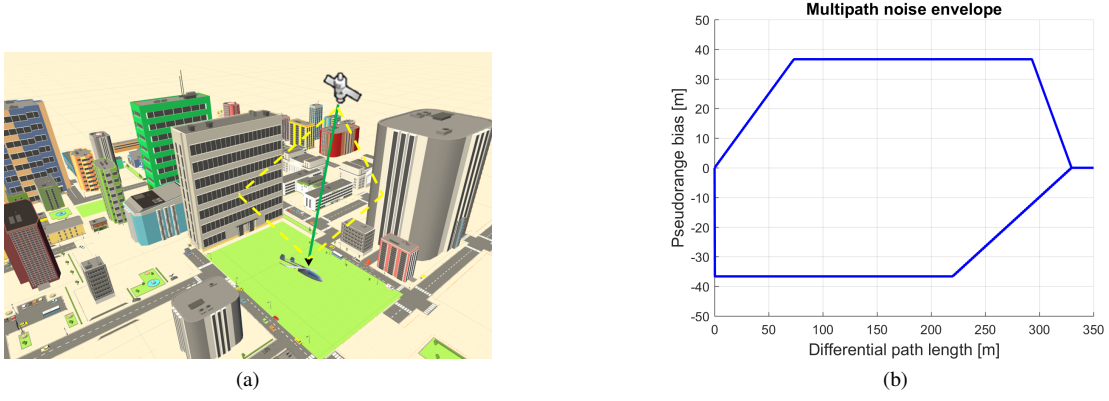


Fig. 5: (a) Simulated urban environment where we perform ray-tracing to compute the differential path lengths between the direct signal (green) and the multipath signals (yellow). (b) Multipath noise envelope for a receiver with a quarter-chip early/late correlator spacing.

where the state vector consists of the 2D position  $(x_1, x_2)$  and the heading angle  $\theta$ , the inputs to the system are the forward velocity  $V$  and the angular velocity  $\omega$ , and  $\Delta t$  is the time-step that we set as 0.2 s. We set the covariance matrix for motion model error  $w_k$  as  $Q = \text{diag}([0.01 \text{ m}^2 \ 0.01 \text{ m}^2 \ 0.001 \text{ rad}^2])$ .

For the sensing model, we consider GNSS pseudorange measurements and heading measurements from an on-board compass. The GNSS pseudorange measurement from the  $i^{\text{th}}$  satellite can be expressed as [13]:

$$\rho_k^{(i)} = r(x_k, x_k^{s_i}) + c\delta t + \nu_k^{(i)}, \quad (37)$$

where  $r$  represents the true range between the receiver position  $x_k$  and satellite position  $x_k^{s_i}$  (which we simulate from publicly available almanac data),  $c\delta t$  is the clock bias error, and  $\nu_k^{(i)} \sim \mathcal{N}(b_k^{(i)}, R_k^{(i)})$ . Here  $\nu_k^{(i)}$  contains both the bounded uncertainty due to additional multipath bias  $b_k^{(i)}$  and the stochastic uncertainty with covariance  $R_k^{(i)}$ . We model the stochastic uncertainty with an elevation-based factor [29], [30] as:  $R_k^{(i)} = \Sigma_\rho / \sin^2(\text{el}^{(i)})$ , where we set  $\Sigma_\rho = 5 \text{ m}^2$ . Since we are primarily concerned with the UAS position states, we assume for simplicity that the receiver clock and the satellite clocks are perfectly synced, i.e. there is zero clock bias error. However, if desired, clock bias states can also be included in the state vector for the trajectory planner. Thus, given  $N$  GNSS satellites, the measurement model for the fixed-wing UAS looks as follows:

$$\underbrace{\begin{bmatrix} z_k^{(1)} \\ \vdots \\ z_k^{(N)} \\ z_k^{(N+1)} \end{bmatrix}}_{z_k} = \underbrace{\begin{bmatrix} r(x_k, x_k^{s_1}) \\ \vdots \\ r(x_k, x_k^{s_N}) \\ \theta_k \end{bmatrix}}_{h(x_k)} + \underbrace{\begin{bmatrix} \nu_k^{(1)} \\ \vdots \\ \nu_k^{(N)} \\ \nu_k^{(N+1)} \end{bmatrix}}_{\nu_k}, \quad (38)$$

where  $z_k^{(i)} = \rho_k^{(i)} \ \forall \ i = 1 \text{ to } N$ , and  $z_k^{(N+1)}$  represents the heading measurement with  $\nu_k^{(N+1)} \sim \mathcal{N}(0, 0.001 \text{ rad}^2)$ . For the multipath bias in the pseudorange measurements, we assume a quarter-chip spacing between the early and late correlators [13]. We perform ray-tracing as shown in Fig. 5(a) and assume that the reflected signal strength can be as strong as the direct LOS signal. Based on these characteristics, we get a multipath noise envelope as shown in Fig. 5(b).

### B. Trajectory Planning Results

Given the above motion and sensing models, we setup a  $1 \text{ km} \times 1 \text{ km}$  wide urban environment to evaluate our trajectory planner. In order to simulate multipath effects, we set the flight altitude to 65 m and include buildings up to 120 m tall. We first consider trajectory planning for a single UAS and show the results in Fig. 6. Buildings taller than the flight altitude are colored orange, whereas buildings shorter than the flight altitude are colored yellow. For constructing the planner graph of kinematically feasible and collision-free trajectories, we use a grid of states with 100 m spacing as shown in Fig. 6(a). Once the graph is constructed, the planner explores the graph to find an optimal trajectory between a given start and goal state. In order to statistically validate the collision safety of the planned trajectory, we simulate 1000 trajectories along the planned trajectory. We observe that all 1000 simulated trajectories remain within the  $3\sigma$  confidence zonotopes of the predicted state uncertainty

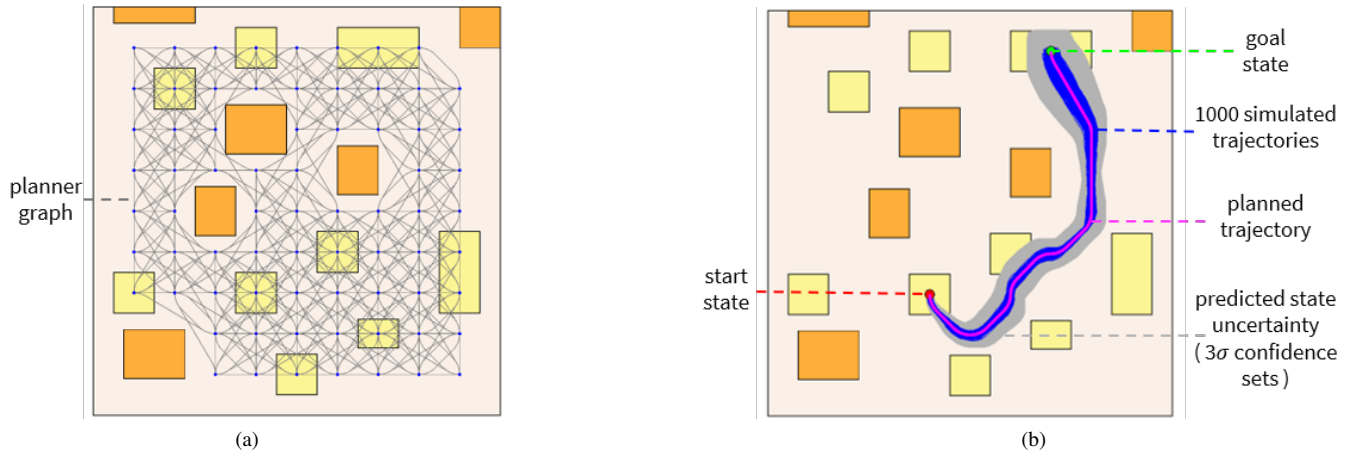


Fig. 6: Planning results for a single fixed-wing UAS. (a) Graph of feasible trajectories built by planner. (b) All 1000 simulated trajectories lie inside the predicted state uncertainty confidence sets, thus validating collision safety of the planned trajectory.

as shown in Fig. 6(b). Thus, the trajectory planner safely leads the UAS to the goal state under stochastic and bounded GNSS uncertainties.

Next, we evaluate the trajectory planner for multiple UAS in a shared airspace. Here we sequentially plan trajectories for five UAS in the same urban environment. Since we assume all UAS to be fixed-wing with the same motion model in Equation (36), the planning framework allows us to reuse the same planner graph constructed in the above scenario. Fig. 7(a) shows the planner graph along with the planned trajectories for the five UAS. The planner begins by finding an optimal trajectory for UAS-1 while maintaining collision safety with respect to the obstacles (orange-colored buildings). Next, the planner finds an optimal trajectory for UAS-2 while maintaining collision safety with respect to UAS-1 and the obstacles. Note that while a shorter candidate trajectory existed for UAS-2, it was rejected by the planner as it could not maintain collision safety with respect to UAS-1. Next, the planner finds an optimal trajectory for UAS-3 while maintaining collision safety with respect to UAS-1, UAS-2, and the obstacles. For UAS-4 the planner finds an optimal trajectory that seems to collide with the trajectory for UAS-2. However, the trajectories do not intersect temporally, thus maintaining collision safety. For UAS-5, we set the same start state as for UAS-4 and set the trajectory start time a few seconds after that of UAS-4. Again the optimal trajectory found by the planner does not intersect temporally with the trajectories for UAS-2 and UAS-4, thus maintaining collision safety. In order to statistically validate the collision safety of the planned trajectories for the five UAS, we simulate 1000 trajectories for each UAS. Figs. 7(b)-(f) show snapshots of the UAS flights with the simulated trajectories and the  $3\sigma$  confidence zonotopes for the predicted state uncertainties. All 1000 simulated trajectories for all the five UAS remain within the  $3\sigma$  confidence zonotopes, thus demonstrating the applicability of the planner to plan collision safe UAS trajectories in a shared airspace.

## VII. CONCLUSIONS

We have presented a trajectory planner that maintains collision safety in the presence of stochastic and bounded sensing uncertainties. We first improved our prior reachability analysis by computing reachable sets as a function of independent quantities. The expression for computing the reachable set was then approximated to predict state uncertainty along the trajectory. Next, we combined our method to predict state uncertainty with a highly parallel trajectory planning framework. We designed a metric for the size of the state uncertainty by obtaining the covariation of its confidence zonotopes. Finally, we demonstrated the applicability of the trajectory planner for GNSS-based navigation of fixed-wing UAS in urban environments. We considered multiple scenarios and statistically validated the collision safety of the planned trajectories.

## REFERENCES

- [1] A. Shetty and G. X. Gao, "Predicting State Uncertainty Bounds Using Non-linear Stochastic Reachability Analysis for Urban GNSS-based UAS Navigation," *IEEE Transactions on Intelligent Transportation Systems*, Accepted, 2020.
- [2] H. Zhou, H. Kong, L. Wei, D. Creighton, and S. Nahavandi, "On Detecting Road Regions in a Single UAV Image," *IEEE transactions on intelligent transportation systems*, vol. 18, no. 7, pp. 1713–1722, 2016.
- [3] R. Ke, Z. Li, S. Kim, J. Ash, Z. Cui, and Y. Wang, "Real-time Bidirectional Traffic Flow Parameter Estimation from Aerial Videos," *IEEE Transactions on Intelligent Transportation Systems*, vol. 18, no. 4, pp. 890–901, 2016.

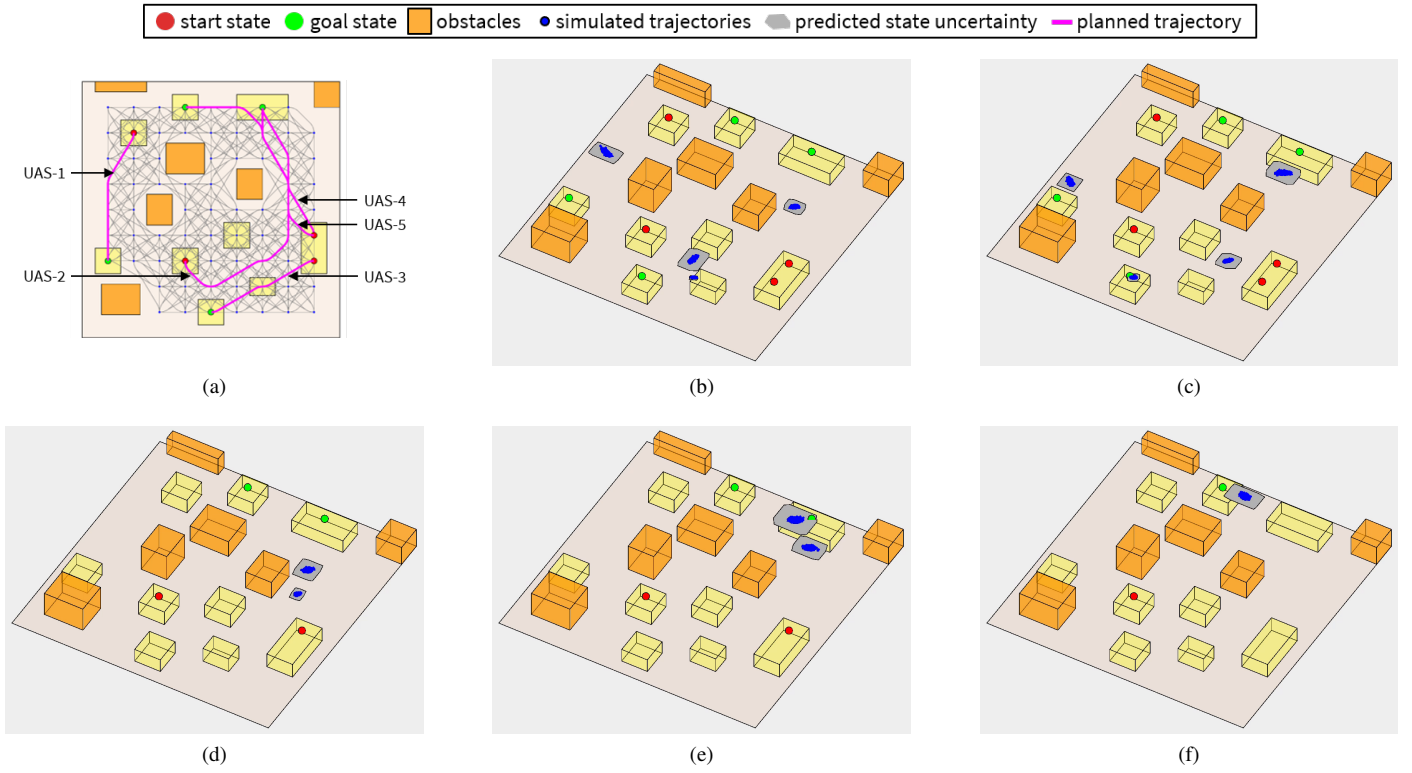


Fig. 7: Planning results for multiple fixed-wing UAS. (a) Planned trajectories for all UAS along with the planner graph. (b)-(f) Snapshots during trajectory execution including 1000 simulated trajectories and predicted state uncertainty confidence sets. The complete video can be found at <https://youtu.be/eyA3vEojdnQ>.

- [4] S. Jwa, Ü. Ozguner, and Z. Tang, "Information-Theoretic Data Registration for UAV-based Sensing," *IEEE Transactions on intelligent transportation systems*, vol. 9, no. 1, pp. 5–15, 2008.
- [5] H. Zhou, H. Kong, L. Wei, D. Creighton, and S. Nahavandi, "Efficient Road Detection and Tracking for Unmanned Aerial Vehicle," *IEEE transactions on intelligent transportation systems*, vol. 16, no. 1, pp. 297–309, 2014.
- [6] Y. Xu, G. Yu, X. Wu, Y. Wang, and Y. Ma, "An Enhanced Viola-Jones Vehicle Detection Method from Unmanned Aerial Vehicles Imagery," *IEEE Transactions on Intelligent Transportation Systems*, vol. 18, no. 7, pp. 1845–1856, 2016.
- [7] S. M. LaValle, *Planning algorithms*. Cambridge university press, 2006.
- [8] S. Karaman and E. Frazzoli, "Sampling-Based Algorithms for Optimal Motion Planning," *The International Journal of Robotics Research*, vol. 30, no. 7, pp. 846–894, 2011.
- [9] J. Van Den Berg, P. Abbeel, and K. Goldberg, "LQG-MP: Optimized Path Planning for Robots with Motion Uncertainty and Imperfect State Information," *The International Journal of Robotics Research*, vol. 30, no. 7, pp. 895–913, 2011.
- [10] A. Bry and N. Roy, "Rapidly-Exploring Random Belief Trees for Motion Planning Under Uncertainty," in *2011 IEEE international conference on robotics and automation*. IEEE, 2011, pp. 723–730.
- [11] D. Claes, D. Hennes, K. Tuyls, and W. Meeussen, "Collision Avoidance Under Bounded Localization Uncertainty," in *2012 IEEE/RSJ International Conference on Intelligent Robots and Systems*. IEEE, 2012, pp. 1192–1198.
- [12] S. Vaskov, U. Sharma, S. Kousik, M. Johnson-Roberson, and R. Vasudevan, "Guaranteed Safe Reachability-based Trajectory Design for a High-fidelity Model of an Autonomous Passenger Vehicle," in *2019 American Control Conference (ACC)*. IEEE, 2019, pp. 705–710.
- [13] P. Misra and P. Enge, "Global Positioning System: Signals, Measurements and Performance Second Edition," *Massachusetts: Ganga-Jamuna Press*, 2006.
- [14] S. Peyraud, D. Bétaille, S. Renault, M. Ortiz, F. Mougél, D. Meizel, and F. Peyret, "About Non-Line-of-Sight Satellite Detection and Exclusion in a 3D Map-Aided Localization Algorithm," *Sensors*, vol. 13, no. 1, pp. 829–847, 2013.
- [15] W. Wen, G. Zhang, and L.-T. Hsu, "Exclusion of GNSS NLOS Receptions Caused by Dynamic Objects in Heavy Traffic Urban Scenarios Using Real-time 3D Point Cloud: An Approach Without 3D Maps," in *2018 IEEE/ION Position, Location and Navigation Symposium (PLANS)*. IEEE, 2018, pp. 158–165.
- [16] A. Shetty and G. X. Gao, "Covariance Estimation for GPS-lidar Sensor Fusion for UAVs," in *Proceedings of the 30th International Technical Meeting of The Satellite Division of the Institute of Navigation (ION GNSS+ 2017)*, 2017, pp. 2919–2923.
- [17] G. Zhang and L.-T. Hsu, "A New Path Planning Algorithm Using a GNSS Localization Error Map for UAVs in an Urban Area," *Journal of Intelligent & Robotic Systems*, vol. 94, no. 1, pp. 219–235, 2019.

- [18] A. Shetty and G. X. Gao, "Trajectory Planning Under Stochastic and Bounded Sensing Uncertainties Using Stochastic Reachability," in *Proceedings of the 33rd International Technical Meeting of The Satellite Division of the Institute of Navigation (ION GNSS+ 2020)*, St. Louis, MO, USA, 2020.
- [19] B. Ichter, E. Schmerling, A.-a. Agha-mohammadi, and M. Pavone, "Real-time Stochastic Kinodynamic Motion Planning via Multiobjective Search on GPUs," in *2017 IEEE International Conference on Robotics and Automation (ICRA)*. IEEE, 2017, pp. 5019–5026.
- [20] M. Althoff, O. Stursberg, and M. Buss, "Safety assessment for stochastic linear systems using enclosing hulls of probability density functions," in *2009 European Control Conference (ECC)*. IEEE, 2009, pp. 625–630.
- [21] M. Althoff, "Reachability Analysis and its Application to the Safety Assessment of Autonomous Cars," Ph.D. dissertation, Technische Universität München, 2010.
- [22] M. Susi, M. Andreotti, M. Aquino, and A. Dodson, "Tuning a Kalman Filter Carrier Tracking Algorithm in the Presence of Ionospheric Scintillation," *GPS Solutions*, vol. 21, no. 3, pp. 1149–1160, 2017.
- [23] P. N. Raanes, M. Bocquet, and A. Carrassi, "Adaptive Covariance Inflation in the Ensemble Kalman Filter by Gaussian Scale Mixtures," *Quarterly Journal of the Royal Meteorological Society*, vol. 145, no. 718, pp. 53–75, 2019.
- [24] Y. Yang and W. Gao, "An Optimal Adaptive Kalman Filter," *Journal of Geodesy*, vol. 80, no. 4, pp. 177–183, 2006.
- [25] G. Costante, C. Forster, J. Delmerico, P. Valigi, and D. Scaramuzza, "Perception-aware Path Planning," *arXiv preprint arXiv:1605.04151*, 2016.
- [26] B. Wang, W. Shi, and Z. Miao, "Confidence Analysis of Standard Deviation Ellipse and its Extension into Higher Dimensional Euclidean Space," *PloS one*, vol. 10, no. 3, p. e0118537, 2015.
- [27] W. E. Hoover, "Algorithms for Confidence Circles and Ellipses," *NOAA Technical Report*, 1984.
- [28] C. Combastel, "Zonotopes and Kalman Observers: Gain Optimality Under Distinct Uncertainty Paradigms and Robust Convergence," *Automatica*, vol. 55, pp. 265–273, 2015.
- [29] S. Tay and J. Marais, "Weighting Models for GPS Pseudorange Observations for Land Transportation in Urban Canyons," 2013.
- [30] H. Hartinger and F. Brunner, "Variances of GPS Phase Observations: The SIGMA-E Model," *GPS solutions*, vol. 2, no. 4, pp. 35–43, 1999.